DISCLAIMER

This report was prepared as an account of work sponsored by an agency of the United States Government. Neither the United States Government nor any agency thereof, nor any of their employees, makes any warranty, express or implied, or assumes any legal liability or responsibility for the accuracy, completeness, or usefulness of any information, apparatus, product, or process disclosed, or represents that its use would not infringe privately owned rights. Reference herein to any specific commercial product, process, or service by trade name, trademark, manufacturer, or otherwise does not necessarily constitute or imply its endorsement, recommendation, or favoring by the United States Government or any agency thereof. The views and opinions of authors expressed herein do not necessarily state or reflect those of the United States Government or any agency thereof. Reference herein to any social initiative (including but not limited to Diversity, Equity, and Inclusion (DEI); Community Benefits Plans (CBP); Justice 40; etc.) is made by the Author independent of any current requirement by the United States Government and does not constitute or imply endorsement, recommendation, or support by the United States Government or any agency thereof.

LA-UR-25-28086

Approved for public release; distribution is unlimited.

Title:	Theoretical Modeling of Reactor Relevant Conditions for Plasma Jet Driven Magneto-Inertial Fusion
Author(s):	Cassibry, Jason Chu, Feng
Intended for:	Report
Issued:	2025-08-07

Theoretical Modeling of Reactor Relevant Conditions for Plasma Jet Driven Magneto-Inertial Fusion

1. Introduction

The Charger Advanced Power and Propulsion Laboratory (CAPP), a laboratory within the Propulsion Research Center (PRC) at the University of Alabama in Huntsville (UAH) is working with Los Alamos National Laboratory (LANL). to develop models and inform on promising paths for high gain magneto-inertial fusion (MIF) conditions. This report provides a framework for identifying promising conditions for achieving ignition in plasma-jet-driven magneto-inertial fusion (PJMIF)[1]. As proposed, for the first part of the contract, UAH proposes to develop a gain over unity set of stagnation conditions to provide a state of plasma conditions to achieve to set long terms goals for the PJMIF program. Specifically, UAH will model PJMIF stagnation conditions to include radiation, heat transfer, two temperature energy equations, fusion reactivity and nonlocal fusion product deposition, but no hydrodynamics for these purposes. These calculations will use a stationary plasma model to reduce simulation complexity—focusing on a DT target at 10 keV. Subsequent work will include a DD plasma layer acting as an afterburner. UAH will assume an initial magnetic field without any consideration of the topology, just assume a field strength, most likely scaled with consideration of the local hall parameter. This effort will inform the team on the tradeoff between mass, peak target field, etc and the achievable gain.

PJMIF is an innovative approach to controlled fusion that bridges the gap between magnetic confinement fusion and inertial confinement fusion. This method utilizes an array of supersonic plasma jets to symmetrically compress a magnetized fuel target, achieving conditions necessary for fusion ignition. The plasma jets, typically generated by pulsed plasma accelerators, provide a

scalable and cost-effective means of compression while mitigating many of the technical challenges faced by traditional approaches. PJMIF is significant because it offers a path toward high energy gain fusion, leveraging the benefits of magnetization to reduce thermal losses while utilizing kinetic compression to reach the necessary temperatures and pressures for fusion reactions. If successful, this approach could enable more compact, lower-cost fusion reactors, revolutionizing both terrestrial energy production and space propulsion applications. As global energy demands continue to rise, PJMIF stands as a promising candidate for achieving practical fusion power, bringing humanity closer to a future of abundant, clean energy.

Before proceeding, this report highlights key concerns about the direction of the fusion community, which shape the framework presented. In December 2022, the National Ignition Facility (NIF) achieved a historic breakthrough in inertial confinement fusion by demonstrating fusion ignition—producing more energy from the reaction than was delivered to the fuel by the laser system[2]. This milestone validated decades of research, confirming that self-sustaining fusion burn is possible in the laboratory. NIF's achievement represents a critical step toward practical fusion energy, reinforcing the viability of inertial confinement approaches while inspiring advancements in alternative fusion methods, including magneto-inertial fusion concepts like plasma-jet-driven compression. While the recent success of the National Ignition Facility (NIF) marks a major milestone in fusion research, traditional inertial confinement fusion (ICF) approaches face significant challenges related to size, cost, and complexity. Facilities like NIF require massive laser arrays, each demanding extreme precision and maintenance, making them prohibitively expensive and impractical for commercial power production. The intricate target fabrication and delivery systems add further engineering challenges, while the sheer scale of these facilities limits their scalability. These concerns have driven interest in alternative methods, such as plasma-jet-driven magneto-inertial fusion (PJMIF), which aims to achieve fusion conditions with a more compact, cost-effective, and potentially scalable approach. Magneto-inertial fusion has traditionally been pursued as a lower-cost, lower-volume alternativeMA[3]. However, modern embodiments such as MagLIF require pulsed currents exceeding 50 MA of total current[4] necessitating complex pulsed power systems with pulse compression and challenging path to high pulse repetition. Alternative: Currently, PJMIF requires hundreds of pulsed plasma accelerators arranged spherically. This design process begins with anticipated stagnation conditions and confinement time, working backward to define liner requirements. Then knowing the mass achievable per plasma accelerator and standoff, determining the final system. It's a system of the order of 100 MJ. This will be quite large, complicated, and expensive to build and maintain. Additionally, if NIF is any indicator, PJMIF will struggle for many years before maturing the technologies needed for the high precision needed for shock heating and spherical compression. While the CAPP laboratory is fully capable of modeling this pathway, this report proposes an alternative PJMIF parameter space aimed at simplifying and reducing the overall reactor size.

The rest of the report is organized as follows. Section 2 presents the theoretical models used in this report, specifically preliminary planning, power balance for stationary plasma states, and analytical states. Results are presented in section 3, followed by discussion and concluding remarks in section 4.

2. Theoretical Models

This section draws upon numerous analytical models of magneto-inertial fusion (MIF). An excellent reference for the inertial physics is the textbook by Atzeni and Meyer-ter-Vehn[5] Among the earliest MIF studies, Lindemuth and Kirkpatrick investigated the impact of magnetic fields on inertial targets, systematically varying density and implosion velocity[6]. Their work was generalized by Kirkpatrick to power balance diagrams as a function of aerial density and fuel temperature [7]. Drake et al demonstrated that targets with an initial density of 10^{24} m^{-3}, magnetic field of ~10 T, and initial temperature of 100 eV could reach ignition and gain over unity with ~100 kJ of initial energy. Similar conclusions about the merits of magnetic fields and preheat were identified by Ribe and Barnes[8] with magnetized impact fusion, Turchi[9] with the Linus concept, and Siemon et al [10] with magnetized target fusion. Deposition of fusion products into magnetized targets in the context of MIF was performed by Basko et al[11]. A critical parameter is the ratio of the target radius to the born-on Larmor radius of the charged fusion products. Other transport properties are documented in the NRL Plasma Formulary[12], with updates on many parameters provided by Davies et al[13]. For plasma liner specific studies, semi-analytic 1D treatments of Mag LIF[14] and Staged Z-pinch[15] were developed and performed. The focus on those studies was the verification of the tools themselves without a thorough exploration of the parameter space. Most recently, Langendorf and Hsu developed a semi-analytic model of PJMIF[16], highlighting the 1D result that gains of 3 to 30 may be possible with initial plasma liner energies of 20-40 MJ.

2.1. Preliminary Planning for Magneto-Inertial Fusion Experiment: Confinement

Gain over unity in ICF and MIF plasmas are informed by the condition that the confinement time needs to exceed the fusion burn time necessary to recover the energy investment, namely the inequality

$$\tau_{conf} \geq \tau_{fus} \tag{1}$$

The fusion burn time comes from a time integration of the fusion reactivity equation, In general, the volumetric fusion power given by

$$\left(\frac{dE}{dt}\right)_{fus} = \frac{n_i n_j}{(1+\delta_{ij})} \langle \sigma v \rangle_{ij} \mathcal{V} E_{fus,ij} \tag{2}$$

where δ_{ij} is 1 if i=j (i.e. D-D, T-T reactions) and 0 otherwise and $\mathcal{V}$ is the target volume. The number density of the fuel with

$$n_i = X_i n \tag{3}$$

where $\sum_{i=1}^{N_{species}} X_i = 1$ are the mole fractions. Typically, the number of species is 2, and deuterium and tritium are the species in proportions of 50% each by mole fraction. For binary reactions involving different species, we the have

$$\left(\frac{dE}{dt}\right)_{fus} = n^2 X_1 (1 - X_1) \langle \sigma v \rangle \mathcal{V} E_{fus} \tag{4}$$

For thermal DT plasmas, neglecting the magnetic field energy, the total energy is

$E_{th}=n\,m_i\,\mathcal{V}\,\frac{R}{\gamma-1}2\,T$. The total energy released from fusion can exceed the thermal energy by almost a factor of 500, so the number density can be approximated as a constant for the sake of rapid order of magnitude analysis, setting up an inequality

$$E_{th}=n\,m_i\,\mathcal{V}\,\frac{R}{\gamma-1}2\,T\le E_b\approx n^2\,X_1(1-X_1)<\sigma\,v>\mathcal{V}\,E_{fus}\tau_b \tag{5}$$

This provides our definition of burn time. So for planning purposes, the time to recover the thermal energy must satisfy

$$\tau_b\ge\left(\frac{2\,m_a\bar{R}}{(\gamma-1)}\frac{1}{X_1(1-X_1)}\right)\left(\frac{T}{<\sigma\,v>E_{fus}}\right)\frac{1}{n} \tag{6}$$

For practical purposes, burn time is inversely proportional to number density, and the temperature, reactivity, and fusion energy per reaction set the scale.

In ICF and MIF, the confinement time is required to exceed the burn time. Confinement time from analytical arguments has historically been a point of contention and should be a focus of future experimental and modeling studies(see e.g. Thio et al [17] vs. Parks [18]). For this model it is assumed that the confinement time is the liner thickness l_L divided by the expansion rate $v_{\exp,L}$, and it is assumed that the expansion rate is based on a fraction of the incoming liner speed, due to the rapid radiative cooling by the high Z materials, leading to liner temperatures of 2-4 eV. Further, we require dynamic pressure to exceed the stagnation and magnetic field pressure of the target, leading to an implosion speed of

$$V_L=\sqrt{\frac{4\,n\,k\,T_T+0.5\,B_T^2/\mu_0}{\rho_L}} \tag{7}$$

where ρ_L is the mass density of the liner. Assuming a liner expansion rate of V_L/M_L leads to the required thickness of the liner,

$$l_L\ge\frac{V_L\,2\,m_a\bar{R}}{M_L(\gamma-1)\,X_1(1-X_1)}\frac{T_T}{<\sigma\,v>n_T\,E_{fus}} \tag{8}$$

The magnetic field is not arbitrary, and can be guided by the ratio of the target radius to the Larmor radius of the born-on alpha particles. Using results from Ref. [11],

$$r_{\alpha,Lar,0}\le\frac{r_T}{3} \tag{9}$$

where r_T is the target radius. This inequality leads to

$$B_T\ge\frac{\sqrt{2\,m_\alpha E_{fus,\alpha 0}}}{2\,q\,r_{\alpha,Lar,0}}; \tag{10}$$

With these parameters defined by the independent variable of n and r_T , everything, including the total mass, energy, and kinetic energy of the liner, can be estimated providing a promising and much narrower selection for initial parameters in an otherwise overwhelmingly large multidimensional parameter space.

2.2. Power balance of an igniting sphere

For the burning target, the first law of thermodynamics gives

$$\frac{dE}{dt} = W_{dep} - W_m - W_r - W_e \tag{11}$$

where W_{dep}, W_m, W_r, and W_e are the powers of fusion product deposition, mechanical work (pdV), radiation, and thermal conduction. We treat each of these terms below.

2.2.1. Fusion power deposition

In general, the volumetric fusion power given by

$$\frac{dE}{dt} \equiv W_{fus} = \frac{n_i n_j}{(1+\delta_{ij})} \langle \sigma v \rangle E_{fus} \mathcal{V} \tag{12}$$

where δ_{ij} is 1 if i=j (i.e. D-D, T-T reactions) and 0 otherwise. In general, the deposition power is given by

$$W_{dep} = W_{fus} f_{dep} = \frac{n_i n_j}{(1+\delta_{ij})} \langle \sigma v \rangle \mathcal{V} \sum_m E_{fus,m} f_m \tag{13}$$

For example, the power density for equimolar DT has already been given as (if $\frac{n}{2} = n_D = n_T$, also noting $\delta_{ij} = 0$),

$$\frac{dE_{DT}}{dt} \equiv W_{fus} = \frac{1}{4} n^2 \langle \sigma v \rangle_{DT} E_{DT} \tag{14}$$

A fraction of this power f_{dep} is deposited within the hotspot. We can write this as

$$W_{dep} = W_{fus} f_{dep} = W_\alpha (f_\alpha + 4 f_n) \tag{15}$$

for DT specifically. For temperatures below 25 to 30 keV, charged particle fusion products slow down mostly due to small angle electron scattering collisions. The velocity decreases according to

$$\frac{dv_\alpha}{dt} = \frac{-v_\alpha}{2 t_{\alpha e}} \tag{16}$$

where $t_{\alpha e}$ is a characteristic time for energy deposition given by

$$t_{\alpha e} \approx \frac{42 T_e^{3/2}}{\rho \ln \Lambda_{\alpha e}} \ [\text{ps}] \tag{17}$$

where T_e is in units of keV and $\ln \Lambda_{\alpha e}$ is the Coulomb logarithm for collisions between alphas and electrons. The range of a 3.5 MeV alpha particle in a homogeneous plasma is obtained as

$$l_\alpha = 2 v_{\alpha 0} t_{\alpha e} \approx 0.107 \frac{T_e^{3/2}}{\rho \ln \Lambda_{\alpha e}} \ [\text{cm}] \tag{18}$$

where $v_{\alpha 0} = 1.29 \times 10^9 \text{ cm/s}$ is the 'born on' velocity of the alpha particles. More conveniently (for me anyway), the approximate formula for l_α is

$$l_\alpha = 1.07 \frac{T_e^{3/2}}{\rho \ln \Lambda_{\alpha e}} \quad \text{m} \tag{19}$$

where ρ is the mass density of the fuel in kg/m^3, T_e is the temperature in keV, and $\ln \Lambda_{\alpha e}$ is the Coulomb logarithm (impact parameter). This value I will explain in class, but is typically about 10.0 regardless of the physics regime. The fraction of the energy deposition by the alpha is

$$f_\alpha = \begin{cases} \frac{3}{2}\tau_\alpha - \frac{4}{5}\tau_\alpha^2 & \tau_\alpha \le 1/2 \\ 1 - \frac{1}{4\tau_\alpha} + \frac{1}{160\,\tau_\alpha^3} & \tau_\alpha \ge 1/2 \end{cases} \tag{20}$$

where $\tau_\alpha = R_h / l_\alpha$ is the ratio of the burning sphere to 'range of α particle' (it means the distance, roughly, over which it travels before losing its energy to collisions).

A magnetic field will enhance the deposition. The most important figure of merit is the ratio of the radius Rh with the Larmor radius of an alpha, which is

$$r_{L\alpha} = \frac{m v_{\perp \alpha 0}}{2 q B} \tag{21}$$

where $v_{\perp \alpha 0}$ is the 'born on' or starting velocity of the alpha particle. This is calculated with

$$E_\alpha = \frac{1}{2} m_\alpha v_{\perp \alpha 0}^2 \tag{22}$$

thus $v_{\perp \alpha 0} = 1.2986 \times 10^7$ m/s .

$$\tau_\alpha = \frac{R_h}{l_\alpha}\left(1 + \frac{R_h}{r_{L\alpha}}\right) \equiv \bar{R}(1+b) \tag{23}$$

The results are shown below for b = 0.1, 1, and 10 to show how the magnetic field can enhance deposition for charged particles. The benefits of the magnetic field can be seen to improve the local deposition and require lower densities as the curve shifts to the upper left.

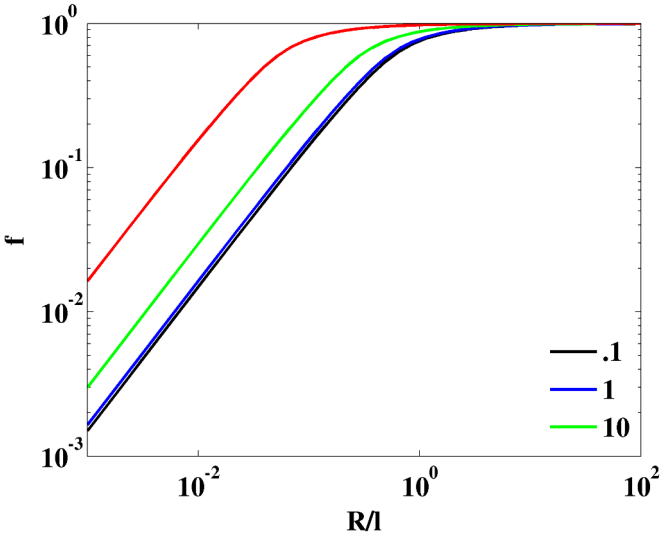

Figure 1. Fractional fusion deposition as a function of target radius to stopping length at fixed value of target radius to born on alpha Larmor radius.

2.2.2. Thermal conduction

Electrons dominate thermal conduction because they are highly mobile. There are three thermal conductivities for electrons, $k_{\parallel}^{e}, k_{\perp}^{e}, k_{\wedge}^{e}$, where the subscript refers to the direction of the conduction with respect to a magnetic field. For the perpendicular component,

$$k_{\perp,e} = \frac{n T_e \tau_e k_B^2}{m_e} \left(\frac{f_{\gamma_1'} x^2 + f_{\gamma_0'}}{\Delta} \right) \left[\frac{\mathrm{W}}{\mathrm{m \cdot K}} \right] \tag{24}$$

where temperature is in K, Z is the charge (1.0 for any combination of fully ionized H, D, and T). The electron collision time τ_e is given by

$$\tau_e = \frac{3\sqrt{m_e}}{4\sqrt{2\pi}} \frac{(k_B T_e)^{(3/2)}}{n_e \lambda} \frac{(4\pi\varepsilon_0)^2}{q^4} \tag{25}$$

n_e is the electron number density in m^{-3}, and m_e is the electron mass in kg. x is the Hall parameter given by

$$x = \omega_e \tau_e = \frac{q B}{m_e} \tau_e \tag{26}$$

where B is the magnetic induction field in Tesla. The coefficient Δ is given by

$$\Delta = x^4 + f_{\delta_1} x^2 + f_{\delta_0} \tag{27}$$

Finally, the four 'f' coefficients are can be interpolated from tabular results in Braginskii[19] by

$$
\begin{aligned}
f_{\gamma_0'} &= 11.92\left(0.10067+\frac{0.58456}{-0.35+Z^{1.1}}\right)\\
f_{\gamma_1'} &= 4.664\left(0.69683+\frac{0.30317}{Z}\right)\\
f_{\delta_0'} &= 3.7703\left(0.025489+\frac{0.63343}{-.35+Z^{3/2}}\right)\\
f_{\delta_1'} &= 14.79\left(0.50588+\frac{0.40765}{-0.175+Z}\right)
\end{aligned}
\tag{28}
$$

Finally, the Coulomb logarithm λ is given by the piecewise function

$$
\lambda = \begin{array}{ll} 29.9-\log\left(\sqrt{n_e}\,T_{eV}^{(-3/2)}\right) & T_{eV}<10 \ \text{eV} \\ 30.9-\log\left(\sqrt{n_e}\,T_{eV}^{(-1)}\right) & T_{eV}\geq 10 \ \text{eV} \end{array}
\tag{29}
$$

These functions are curve fit to a table of data to account for the effect of variable charge state of the heavy ion particles. The curve fits were determined by me in my dissertation work.

Similarly for ions, we have

$$
k_{\perp,i} = \frac{n\,T_i\,\tau_i\,k_B^2}{m_a\,MW_i}\left(\frac{2\,x_i^2+2.645}{\Delta_i}\right)\left[\frac{\text{W}}{\text{m}\cdot\text{K}}\right]
\tag{30}
$$

where T_i is the ion temperature in K. The ion collision time τ_i is given by

$$
\tau_i = \frac{3\sqrt{m_e}}{4\sqrt{\pi}}\frac{\left(k_B T_i\right)^{(3/2)}}{n_i\lambda}\frac{\left(4\pi\varepsilon_0\right)^2}{q^4}
\tag{31}
$$

n_i is the ion number density in m^{-3}, and m_e is the electron mass in kg. x_i is the ion Hall parameter given by

$$
x_i = \omega_i\,\tau_i = \frac{q\,B}{m_a\,MW_i}\,\tau_i
\tag{32}
$$

The coefficient Δ_i is given by

$$
\Delta_i = x_i^4 + 4.03\,x_i^2 + 2.33
\tag{33}
$$

Since heat transfer rates are dominated by the electrons, we will focus our calculations using electron transport and neglect ions for now. The thermal conduction power on average can be modeled with

$$
W_e = -k_e\nabla T_e S
\tag{34}
$$

We can approximate the gradient as $\nabla T_e \approx T_e / r_T$, and using the equation above accounting for magnetic fields with temperature in eV and using the spherical geometry

$$W_e = -\frac{9.6958\times10^3 T_{e,eV}^{5/2}}{Z\ln\Lambda}\left(\frac{f_{y_1'}x^2+f_{y_0'}}{\Delta}\right)\frac{T_{e,eV}\,4\pi R_h^2}{R_h\,4/3\,\pi R_h^3}\mathcal{V}$$
$$= -\frac{2.91\times10^4 T_{e,eV}^{7/2}}{Z\ln\Lambda\, R_h^2}\left(\frac{f_{y_1'}x^2+f_{y_0'}}{\Delta}\right)\mathcal{V} \quad (35)$$

2.2.3. Bremsstrahlung

Bremsstrahlung power per unit volume is[20]

$$P_{br} = \frac{-\mathcal{V}16\pi}{3\sqrt{6\pi}}\frac{q^6}{m_e^2c^3(4\pi\varepsilon_0)^3}\frac{Z_i^2 n_e\rho}{\sqrt{k_B T_{e,K}/m_e}\,MW_i m_a}\int_0^\infty 4\pi\exp\frac{-h\nu}{k_B T_{e,K}}d\nu$$
$$= \frac{-\mathcal{V}64\pi^2}{3\sqrt{6\pi}}\frac{q^6}{m_e c^2 h(4\pi\varepsilon_0)^3}\sqrt{\frac{k_B T_{e,K}}{m_e c^2}}\frac{Z_i^3\rho^2}{(MW_i m_a)^2} \quad (36)$$
$$= \mathcal{V}4.856\times10^{-37} n_i^2 T_{e,keV}^{1/2} Z_i^3$$

where the temperature units are given by the subscript.

2.2.4. Mechanical Work

The mechanical work is sometimes called the compressional or pdV work. On a per unit volume basis, this term is

$$W_m = p_h\frac{dV}{dt} \quad (37)$$

For a sphere,

$$\frac{dV}{dt} = \frac{4}{3}\pi 3 R_h^2\frac{dR_h}{dt} = 4\pi R_h^2 u \quad (38)$$

where u is the implosion velocity. Thus

$$W_m = 4\pi r_T^2 u\rho_T R T_T \quad (39)$$

where R is the gas constant for the plasma. For isobaric ignition, the pressures match across the hotspot boundary and u = 0.

2.3. Hot spot evolution and burn propagation

Energy conservation in the burning region is

$$M\frac{de}{dt} = (W_{cp}f - W_b - W_e)V - pSu_{\exp} - e\frac{dM}{dt} \quad (40)$$

where the surface area is given by

$$S = \begin{cases} 4\pi r^2 & \text{spherical} \\ 2\pi r l & \text{cylindrical} \end{cases} \quad (41)$$

M mass of the hotspot, e M is the energy of the hotspot, ρ_c is the density of the cold fuel surrounding the hotspot, p, pressure inside the burning hotspot, u velocity, where there are two distinct velocities, u_{bw} and u_{exp}, where bw means burn wave and exp means expansion.

The rate of mass accretion (mass increase in the hotpot), is evaluated assuming that is the rate at which the surrounding cold material heats up to an energy e matching the hotpot value. The heating comes from two terms, the charged particles not deposited in the hotspot, and the thermal conduction into the cold layer,

$$e\frac{dM}{dt}=[W_{cp}(1-f_{cp})+W_e]V \tag{42}$$

Total energy E is

$$E=eM \tag{43}$$

where e is the specific internal energy,

$$e=C_vT=\frac{\bar{R}}{MW(\gamma-1)}(T_e+T_i) \tag{44}$$

The volume depends on the geometry of the target,

$$\mathcal{V}=\begin{cases}\frac{4}{3}\pi r^3 & \text{spherical}\\ \pi r^2 l & \text{cylindrical}\end{cases} \tag{45}$$

The burn wave velocity can be obtained in terms of the time rate of change of mass of the system, since

$$r=\begin{cases}\left(\frac{M}{\rho}\frac{3}{4\pi}\right)^{(1/3)} & \text{spherical}\\ \left(\frac{M}{\rho}\frac{1}{l\pi}\right)^{(1/2)} & \text{cylindrical}\end{cases} \tag{46}$$

The burnwave velocity is

$$\frac{dr}{dt}\equiv u_{bw}=\begin{cases}\frac{1}{4\pi\rho}\left(\frac{M}{\rho}\frac{3}{4\pi}\right)^{(-2/3)}\frac{dM}{dt} & \text{spherical}\\ \frac{1}{2\pi\rho l}\left(\frac{M}{\rho}\frac{1}{l\pi}\right)^{(-1/2)}\frac{dM}{dt} & \text{cylindrical}\end{cases} \tag{47}$$

The pressure is then approximated with ideal gas, unless the density gets to be too high.

$$P=n_ikT_i+n_ekT_e \tag{48}$$

These equations give a pair for ordinary differential equations that need to be integrated in time, along with a lot of models that are plugged into these equations for all the various terms. The model here uses blast wave theory to estimate the expansion speed, and is summarized in the next section.

3. Results

3.1. Scope of Work

The modeling was performed to guide the multidimensional modeling to follow in the midterm and final report using SPFMax[21], [22]. The first set of results come from section 2.1 in which the burn time and various constraints in which target density and radii are independently varied, and the burn time, magnetic field, plasma liner velocity, liner thickness, total mass, and total kinetic energy. These results provide guidance on initial and stagnation conditions which may lead to ignition and gain over unity. Further insights can be gained by plotting contours of net heating and cooling using the fusion power balance equations of section 2.2. These results inform on target radius, density, and magnetic field, used to perform a point design computation of the hot spot evolution as a way to verify the usefulness of guiding models from the previous sections.

3.2. Effects of Burn Time and Local α Deposition Constraints on the Liner

The burn time, neglecting transport effects, is independent of scale and inversely proportional to density as shown in the figure below plotted from 10^{25} to 10^{28} m^{-3}. Across this space, the time varies from ~10 μs down to 20 ns. This result is useful for estimating both the burn time of the target and of the afterburner. Analytical modeling tends to focus on the target, which puts constraints on the liner thickness as shown later. Results tend to require thicker liners requiring higher energy drivers. However, if the afterburner can ignite via heat transfer and fusion product transfer from the target, the target's role can shift from high yield to spark ignition, which may reduce the liner kinetic energy by an order of magnitude.

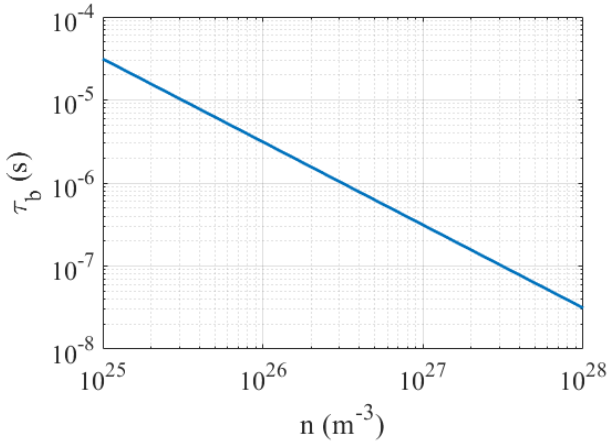

Figure 2. Deuterium tritium burn time vs number density.

The corresponding minimum magnetic field required for local deposition and β are plotted. The magnetic field is only a function of the target radius, if set by the born on radius of the alpha particles. The ratio of thermal to magnetic field pressure ranges from fully magnetized (low β) to negligible. Typical target radii of 10 mm and densities of 10^{26} to 10^{27} m^{-3} tend to place β between 10 and 100.

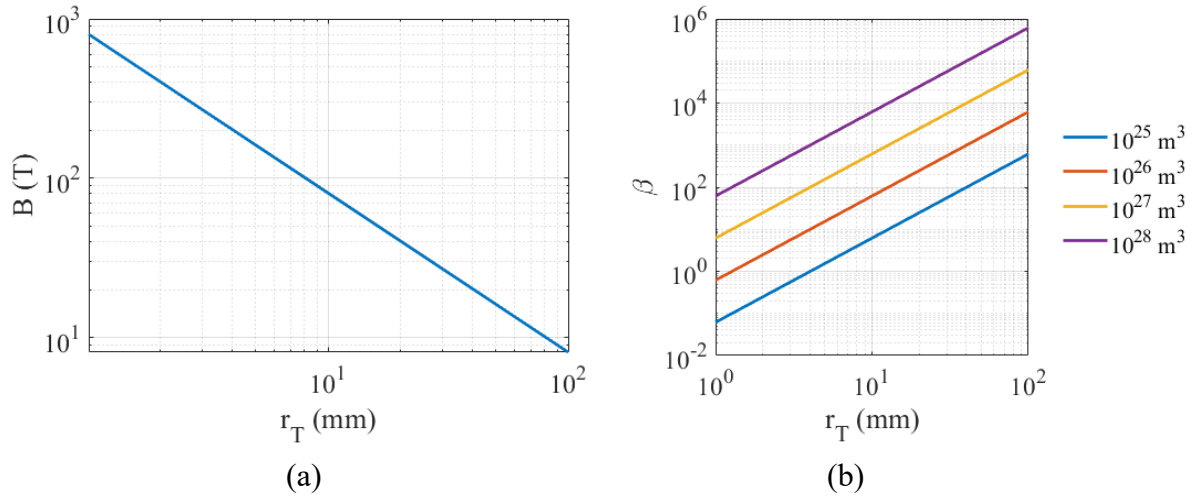

(a) (b)

Figure 3. (a) Minimum magnetic field needed to promote localized burn and (b) corresponding β at fixed value of target number density.

Next we present liner velocity, liner thickness, liner kinetic energy, and number of plasma guns required. Each plot is repeated for liner mass densities of 10, 100, and 1000 kg/m^3. Railguns are recommended for the liner because they can handle significantly higher mass per shot. It is assumed that each railgun can be filled with 1 g of material. The concerns against railguns include impurities from the sidewalls and possibly slower final velocity. In the short term, the value of the PJMIF concept lies not in its potential for cost-competitive electricity, but in its ability to deliver high-yield shots for medical isotope generation, fusion relevant burn conditions for materials and technology development and code validation, and possibly propulsion for cislunar space. These applications do not benefit from the added complexity of using hundreds of coaxial plasma guns.

The minimum liner velocity is plotted as a function of target radius at fixed values of target ion density for three liner mass densities. Liner velocity remains nearly constant across target radii, except at small radii where magnetic field pressure dominates to maintain local alpha deposition constraints. The required liner velocity increases with higher ion target densities and decreases with higher plasma liner densities.

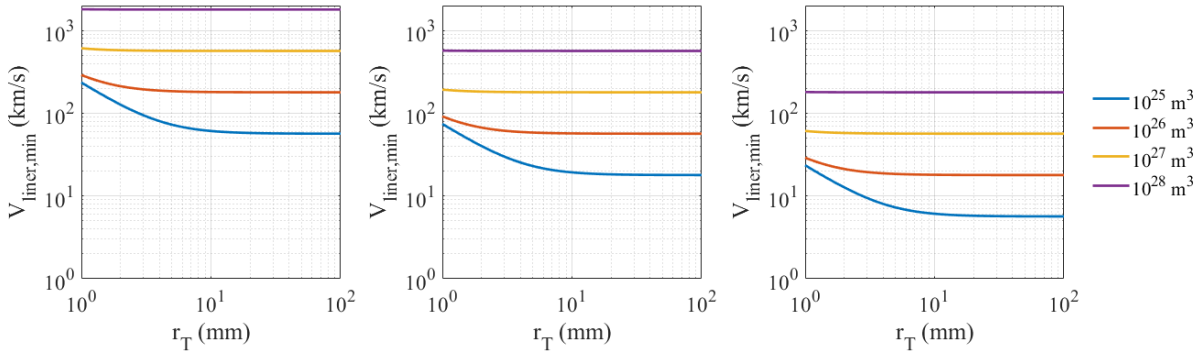

(a) (b) (c)

Figure 4. Minimum liner velocity for confinement at fixed values of ion target density for liner mass densities (ρ_L) of (a) 10 (b) 100, and (c) 1000 kg/m^3.

The minimum liner thickness is plotted as a function of target radius at fixed values of target ion density for three liner mass densities. Liner thickness, like liner velocity, remains nearly constant across target radii, except at small radii and low target ion densities where magnetic field pressure dominates to maintain local alpha deposition constraints. The required liner thickness decreases with higher ion target densities and/or higher plasma liner densities.

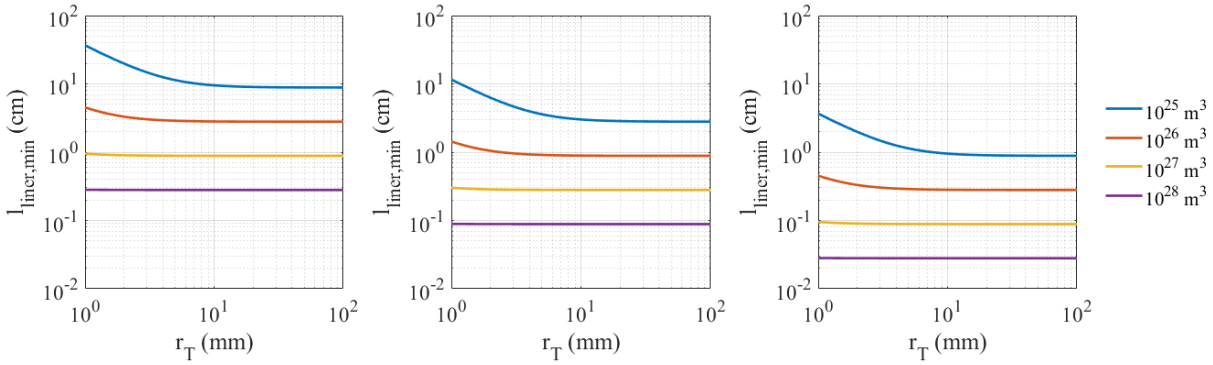

(a) (b) (c)

Figure 5. Minimum liner thickness for confinement at fixed values of ion target density for liner mass densities (ρ_L) of (a) 10 (b) 100, and (c) 1000 kg/m^3.

The minimum liner kinetic energy is plotted as a function of target radius at fixed values of target ion density for three liner mass densities. Liner kinetic energy increases with target radius except when the magnetic field pressure becomes comparable to the target thermal pressure. For lower densities there is a target radius which minimizes the required kinetic energy. In all cases, the liner kinetic energy decreases with increasing liner mass density.

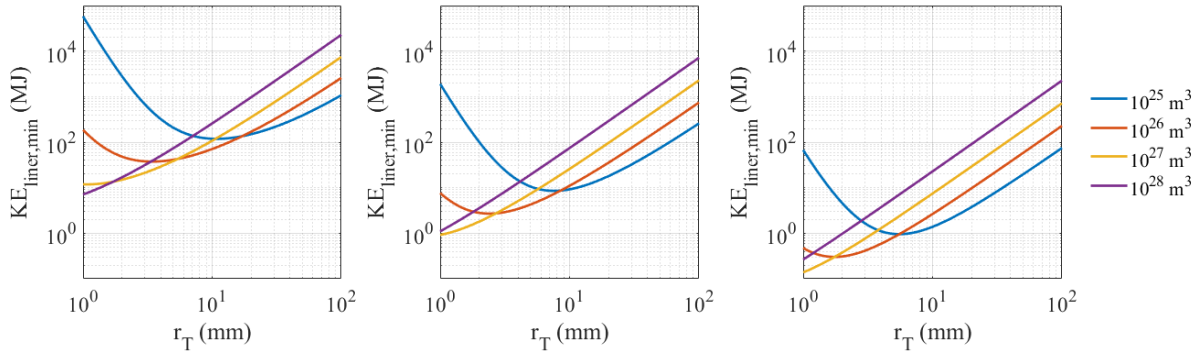

(a) (b) (c)

Figure 6. Minimum liner kinetic energy for confinement at fixed values of ion target density for

liner mass densities (ρ_L) of (a) 10 (b) 100, and (c) 1000 kg/m^3.

The minimum number of railguns, assuming 1 g per gun, is plotted as a function of target radius at fixed values of target ion density for three liner mass densities. The number of guns decreases with target density, because the shorter confinement time of higher density targets reduces the need for thicker liners. At low target densities, the number of required guns minimizes as a function of target radius. Increased target density decreases the number of required guns. The liner mass density has a marginal effect on the number of guns required.

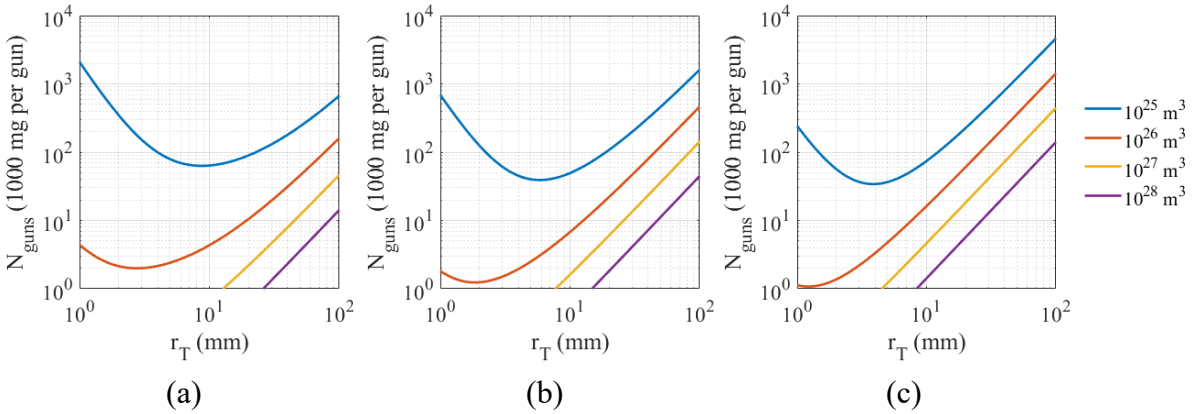

Figure 7. Minimum number of railguns needed for confinement at fixed values of ion target density for liner mass densities (ρ_L) of (a) 10 (b) 100, and (c) 1000 kg/m^3.

3.3. Fusion Power Balance as a Guide for Compressing along a Net Heating Path

To help narrow the parameter space for PJMIF, specifically how to reach the conditions listed above, we can use power balance diagrams, changing parameters such as target radius and implosion velocity, to estimate conditions that might reach ignition by compressing through a net heating parameter space. Below we have a sequence of three power balance plots in a *cylindrical* geometry. Each plot is a contour plot of net heating or cooling with the boundary between each represented by a dashed line. The y axis represents the target temperature in kEv and the x axis is the ion number density for a 50/50 deuterium tritium mixture. Reading left to right, the target radius is 10, 5, and 1 cm. The implosion velocity in each plot is 50, 50, and 5 km/s, respectively, where the velocity is deliberately 10% of the previous two plots anticipating that as a target nears maximum compression the liner will decelerate rapidly. The radius itself enters into shape of the heating contours through transport physics, specifically thermal conduction and fusion deposition. First of all the temperature gradient across the target boundary is assumed to scale as the temperature divided by the radius, following Ref. [7]. However the total heat flux across a surface depends on the surface area, which itself is a function of radius so these effects compete against each other. Finally the fusion deposition depends on the ratio of the target radius to Larmor radius as discussed in section 2 as found in Ref. [11] and is not just assumed that the products are deposited locally. What is apparent from these plots is that cylindrical compression which may be easier in near term testing and target compression, given the inherent cylindrical symmetry of magnetic fields, along with modest compression rates of 10's of km/s, may reach breakeven if the parameters are chosen carefully.

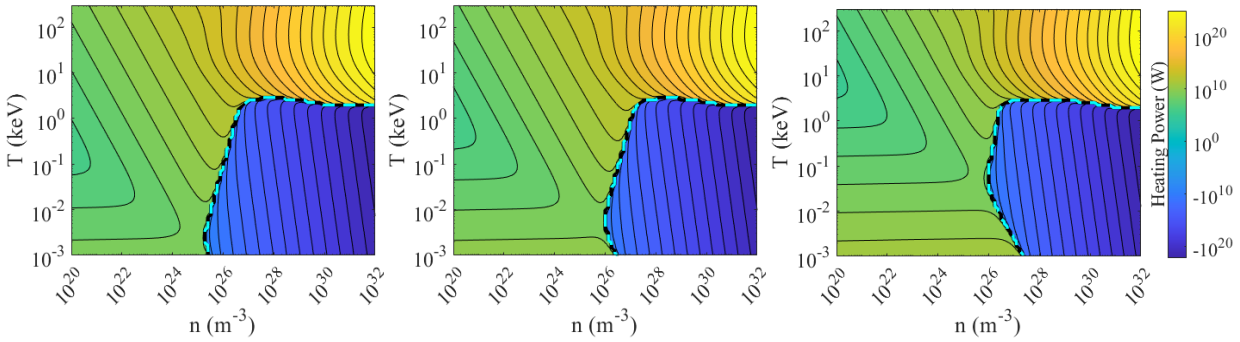

Figure 8. Fusion power balance for BT = 50 T and (a) $r_T = 10\,cm, v_L = 50\,km/s$ *(b)* $r_T = 5\,cm, v_L = 50\,km/s$ *, and (c)* $r_T = 1\,cm, v_L = 5\,km/s$.

The final thermal energy in the target is extremely sensitive to the target radius and stagnation density, Fig. 9. At fixed ion density, the thermal energy scales with r_T^3 . This scaling holds true for both spherical and cylindrical targets, assuming the cylindrical target elongation is held fixed. So, for example, a 10 keV 1 cm target at 10^{26} m^{-3}, would contain 2 MJ of thermal energy, while a 0.5 cm target would only have 250 kJ. To put that into perspective, a 10 kJ high voltage capacitor may have a mass of 100 kg. This is the difference of 20 mT vs 2.5 mT. Assuming a 10% efficiency of transferring stored energy to thermal energy, a reactor might need 2.5 MJ of capacitors instead of 20 MJ by lowering the final target radius by a factor of 2. Our own laboratory has roughly 2 MJ of high voltage capacitors, and so do several of our colleagues.

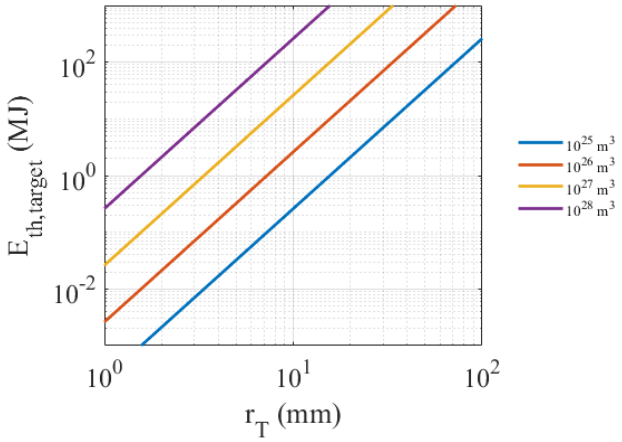

Figure 9. Thermal energy in a 10 keV DT target vs target radius and ion density.

3.4. Point Design Burn Calculation

Building on the guidance from the preceding sections, a point design calculation is performed for at target with 0.5 cm initial radius, 50 T magnetic field, and 10^{26} m^{-3} ion density. The target

reaches unity gain on the order of 1 μs. The next step is to explore the conditions under which a secondary liner can fuel this burn and propagate, amplifying the gain.

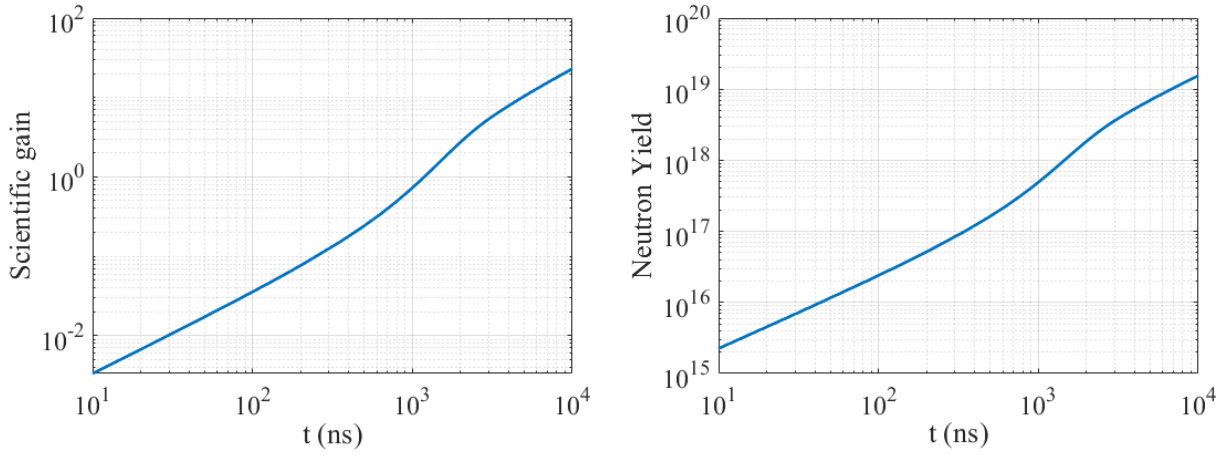

Figure 10. Scientific gain and neutron yield vs burn time for a 0.5 cm target with 50 T magnetic field, $1\times10^{26}\,m^{-3}$ target density, 10 keV temperature.

4. Conclusions

This report explores the feasibility of plasma-jet-driven magneto-inertial fusion (PJMIF) through theoretical modeling and parameter space exploration. By analyzing key constraints on confinement time, burn time, liner dynamics, and fusion power balance, we have identified a path toward achieving ignition and gain with a relatively compact, efficient system.

The analysis highlights several guiding principles:

1. Increased liner density substantially reduces the kinetic energy required for compression, enabling fusion-relevant conditions at sub-megajoule energy scales.
2. Optimal target parameters, including an ion density of 10^{24} to 10^{25} m^{-3}, an initial radius of ~10 cm, and a compression velocity of ~50000 m/s, offer achievable ignition conditions within the parameter space studied.
3. Of critical importance is constraining magnetic field so that the born on Larmor radius is smaller than that of the target at peak compression. Field of 50-100 T for stagnation conditions provide a practical goal. Simultaneously, the plasma β at these conditions is considerably above unity, which may avoid MHD instabilities.
4. The coupling between liner pressure and target internal pressure (thermal plus magnetic field) is critical for maintaining compression and enabling burn propagation, with magnetic field effects playing a key role in energy deposition and confinement.
5. Soft recommendations include the use of railguns for plasma liner formation, and emphasis on short-term fusion applications, such as medical isotope production and fusion relevant conditions for materials and technology development and maturation. Insights gained from near term success can feed into longer-term development of a fusion power plant.

Through power balance analysis and a point design ignition calculations, we demonstrate that

gain exceeding unity is achievable with a 10 MJ system or smaller. Furthermore, the study indicates that the target design can be simplified by relaxing the requirement for direct gain production, instead focusing on igniting a cold fuel layer. This approach has the potential to significantly reduce the overall size and complexity of the reactor system, opening avenues for experimental validation.

Future work will focus on refining the physics of cold fuel layer burn propagation and exploring experimental methods for achieving the necessary initial conditions. This analysis will extend into 3D simulations using SPFMax. This includes investigating liner-driver coupling, the impact of railgun-produced liners on compression uniformity, and optimizing parameter spaces for ignition and energy gain.

In conclusion, PJMIF remains a promising pathway for achieving fusion ignition and gain with significant potential for advancing both terrestrial and space propulsion applications. By addressing the challenges outlined and pursuing the recommendations made in this report, we move closer to realizing the vision of compact, cost-effective fusion energy.

5. Appendix A. Blast wave theory for estimating expansion speed of a hotspot

In blast wave theory[23], the most general form of the equation for the shock radius is given by

$$R_s(t) = \left(\frac{E\, t^2}{\alpha\, A} \right)^{\frac{1}{\nu + 2 - \omega}} \tag{49}$$

where R_s is the shock radius as a function of time t, E is the energy released, A is a constant related to the density profile, α is a normalization constant, ν is the symmetry (1, 2, or 3 for planar, cylindrical, or spherical symmetry), and ω is a free parameter. We also need the time derivative of the shock radius,

$$\dot{R}_s(t) = \frac{2\, R_s(t)}{(\nu + 2 - \omega)\, t} \tag{50}$$

The equations describing the solution depending on ω, and setting $\omega = 0$ gives the case for an explosion into a uniform atmosphere. We will present the results for that case. The undisturbed density is given as a function of the spatial coordinate r as

$$\rho_0(r) = A r^{-\omega} \tag{51}$$

and α is a normalization constant determined later.

Now, we first have to get the nondimensional solution, and then we can calculate the physical pressure, temperature, density, and velocity. The dimensionless variables are

$$\xi = \frac{r}{R_s(t)} \tag{52}$$

The density, velocity, and pressure are nondimensionalized against the shock values,

$$D(\xi) = \frac{\rho(r, t)}{\rho_s} \tag{53}$$

$$V(\xi)=\frac{v(r,t)}{v_s} \tag{54}$$

$$P(\xi)=\frac{p(r,t)}{p_s} \tag{55}$$

Here the equations are presented in the order they need to be calculated, not the order presented in Ref. [23].

$$\omega_1=\frac{3\nu-2+\gamma(2-\nu)}{\gamma+1} \tag{56}$$

$$\omega_2=\frac{2(\gamma-1)+\nu}{\gamma} \tag{57}$$

$$\omega_3=\nu(2-\gamma) \tag{58}$$

$$\beta_0=\frac{1}{\nu\gamma-\nu+2} \tag{59}$$

$$\beta_6=\frac{2}{\nu+2-\omega} \tag{60}$$

$$\beta_7=\omega\beta_6 \tag{61}$$

$$\beta_8=\nu\beta_6 \tag{62}$$

$$\beta_2=\frac{\gamma-1}{\gamma(\omega_2-\omega)} \tag{63}$$

$$\beta_3=\frac{\nu-\omega}{\gamma(\omega_2-\omega)} \tag{64}$$

$$\beta_1=\beta_2+(\gamma+1)\beta_0-\beta_6 \tag{65}$$

$$\beta_4=\beta_1\frac{(\nu-\omega)(\nu+2-\omega)}{\omega_3-\omega} \tag{66}$$

$$\beta_5 = \frac{2\nu - \omega(\gamma+1)}{\omega_3 - \omega} \tag{67}$$

$$C_0 = 2^{\nu}\,\pi^{(\nu-1)/2}\,\frac{\Gamma\left((\nu+1)/2\right)}{\Gamma(\nu)} \tag{68}$$

$$C_5 = \frac{2}{\gamma - 1} \tag{69}$$

$$C_6 = \frac{\gamma+1}{2} \tag{70}$$

$$C_4 = (\nu + 2 - \omega)\,\beta_0\, C_6 \tag{71}$$

$$C_1 = \gamma\, C_5 \tag{72}$$

$$C_2 = \frac{C_6}{\gamma} \tag{73}$$

$$C_3 = \frac{\nu\gamma - \nu + 2}{(\omega_1 - \omega)\,C_6} \tag{74}$$

Now, the solution starts with setting up a vector F that varies from C_2 to 1. So, let

$$dF = (1 - C_2)/100 \tag{75}$$

then

$$F = [C_2 : d\,F : 1] \tag{76}$$

Now we can obtain the dimensionless solution. The dimensionless radius is

$$\xi = F^{-\beta_6}\left[C_1(F - C_2)\right]^{\beta_2}\left[C_3(C_4 - F)\right]^{-\beta_1} \tag{77}$$

Density is

$$D = F^{\beta_7}\left[C_1(F - C_2)\right]^{\beta_3 - \omega\beta_2}\left[C_3(C_4 - F)\right]^{\beta_4 + \omega\beta_1}\left[C_5(C_6 - F)\right]^{-\beta_5} \tag{78}$$

Velocity is

$$V = \xi\, F \tag{79}$$

and pressure is

$$P = F^{\beta_8}\left[C_3(C_4 - F)\right]^{\beta_4 + (\omega-2)\beta_1}\left[C_5(C_6 - F)\right]^{1-\beta_5} \tag{80}$$

The constant that appears in Eq. 49 can now be evaluated with

$$\alpha = \frac{8\,C_0}{(\gamma^2 - 1)(\nu + 2 - \omega)^2}\int_0^1 \xi^{\nu-1}(D\,V^2 + P)\,d\,\xi \tag{81}$$

To do this numerically, here is an example of 2 lines of code to achieve this in Matlab:

```
alfun = 8*C0 /((g^2-1)*(nu+2-omega)^2) .*xsi.^(nu-1) .*(D.*V.^2 + P);
alpha = trapz(xsi,alfun);
```

Now the shock radius and its time derivative can be evaluated, Eqs. 49 and 50. Then,

$$\rho_s = \frac{\gamma+1}{\gamma-1}\rho_0 \tag{82}$$

$$v_s(t) = \frac{2\dot{R}_s(t)}{\gamma+1} \tag{83}$$

$$p_s(t) = \frac{2\rho_0 \dot{R}_s(t)^2}{\gamma+1} \tag{84}$$

Finally, the physical variables are

$$\rho(r,t) = \rho_s D(\xi) \tag{85}$$

$$v(r,t) = v_s(t) V(\xi) \tag{86}$$

6. References

[1] A. L. LaJoie *et al.*, "Formation and Study of a Spherical Plasma Liner for Plasma-Jet-Driven Magneto-Inertial Fusion," Feb. 20, 2024, *arXiv*: arXiv:2401.11066. doi: 10.48550/arXiv.2401.11066.

[2] H. Abu-Shawareb *et al.*, "Achievement of Target Gain Larger than Unity in an Inertial Fusion Experiment," *Phys. Rev. Lett.*, vol. 132, no. 6, p. 065102, Feb. 2024, doi: 10.1103/PhysRevLett.132.065102.

[3] R. E. Siemon *et al.*, "The Relevance of Magnetized Target Fusion (MTF) to Practical Energy Production," Los Alamos, white paper LA-UR-99-2956, Jun. 1999.

[4] S. A. Slutz and R. A. Vesey, "High-Gain Magnetized Inertial Fusion," *Phys. Rev. Lett.*, vol. 108, no. 2, p. 025003, Jan. 2012, doi: 10.1103/PhysRevLett.108.025003.

[5] S. Atzeni and J. Meyer-ter-vehn, *The Physics of Inertial Fusion*. Oxford: Clarendon Press, 2004.

[6] I. R. Lindemuth and R. C. Kirkpatrick, "Parameter Space for Magnetized Fuel Targets in Inertial Confinement Fusion," *Nucl. Fusion*, vol. 23, p. 263, 1983.

[7] R. Kirkpatrick, "Magnetized target fusion. An overview," *Fusion Technol.*, vol. 27, no. 3, pp. 201-201–214, 1995.

[8] F. L. Ribe and D. C. Barnes, "Review of impact fusion concepts (EM launchers)," *IEEE Trans. Magn.*, vol. 25, no. 1, pp. 20–26, Jan. 1989, doi: 10.1109/20.22498.

[9] P. J. Turchi, S. D. Frese, and M. H. Frese, "Stabilized Liner Compressor for Low-Cost Controlled Fusion at Megagauss Field Levels," *IEEE Trans. Plasma Sci.*, vol. 45, no. 10, pp. 2800–2809, Oct. 2017, doi: 10.1109/TPS.2017.2702625.

[10] R. E. Siemon, I. R. Lindemuth, and K. F. Schoenberg, "Why Magnetized Target Fusion Offers a Low-Cost Development Path for Fusion Energy," *Comments Plasma Phys. Control.*

Fusion, vol. 18, no. 6, p. 363, 1999.
[11] M. M. Basko, A. J. Kemp, and J. Meyer-ter-Vehn, "Ignition conditions for magnetized target fusion in cylindrical geometry," *Nucl. Fusion*, vol. 40, no. 1, pp. 59–68, 2000.
[12] J. D. Huba, "NRL: Plasma Formulary," NAVAL RESEARCH LAB WASHINGTON DC BEAM PHYSICS BRANCH, NAVAL RESEARCH LAB WASHINGTON DC BEAM PHYSICS BRANCH, NRL/PU/6790--04-477, Dec. 2004. Accessed: Dec. 31, 2015. [Online]. Available: http://www.dtic.mil/docs/citations/ADA429448
[13] J. R. Davies, H. Wen, J.-Y. Ji, and E. D. Held, "Transport coefficients for magnetic-field evolution in inviscid magnetohydrodynamics," *Phys. Plasmas*, vol. 28, no. 1, p. 012305, Jan. 2021, doi: 10.1063/5.0023445.
[14] R. D. McBride and S. A. Slutz, "A semi-analytic model of magnetized liner inertial fusion," *Phys. Plasmas*, vol. 22, no. 5, p. 052708, May 2015, doi: 10.1063/1.4918953.
[15] J. Narkis *et al.*, "A semi-analytic model of gas-puff liner-on-target magneto-inertial fusion," *Phys. Plasmas*, vol. 26, no. 3, p. 032708, Mar. 2019, doi: 10.1063/1.5086056.
[16] S. J. Langendorf and S. C. Hsu, "Semi-analytic model of plasma-jet-driven magneto-inertial fusion," *Phys. Plasmas*, vol. 24, no. 3, p. 032704, Mar. 2017, doi: 10.1063/1.4977913.
[17] Y. C. F. Thio and Ronald. C. Kirkpatrick, "Magnetized Target Fusion Driven by Plasma Liners," in *Annual Meeting of the American Nuclear Society*, Hollywood, Florida, 2002.
[18] P. Parks, "On the efficacy of imploding plasma liners for magnetized fusion target compression," *Phys. Plasmas*, vol. 15, no. 6, pp. 062506–1 to 062506–12, 2008.
[19] S. I. Braginskii, "Transport Processes in a Plasma," in *Reviews of Plasma Physics*, vol. 1, M. A. Leontovich, Ed., New York: Consultants Bureau, 1965, pp. 205–311.
[20] R. J. Goldston and P. H. Rutherford, *Introduction to Plasma Physics*. Bristol and Philadelphia: Institute of Physics Publishing, 1997.
[21] K. Schillo, J. Cassibry, M. Rodriguez, and S. Thompson, "Suite for Smooth Particle Hydrodynamic Code Relevant to Spherical Plasma Liner Formation and Implosion," *J. Nucl. Eng. Radiat. Sci.*, vol. 5, no. 4, p. 042201, Oct. 2019, doi: 10.1115/1.4042710.
[22] K. Schillo and J. Cassibry, "Effects of initial conditions and transport on ram pressure, Mach number, and uniformity for plasma liner formation and implosion," *Phys. Plasmas*, vol. 27, no. 4, p. 042707, Apr. 2020, doi: 10.1063/1.5143009.
[23] D. L. Book, "The Sedov self-similar point blast solutions in nonuniform media," *Shock Waves*, vol. 4, no. 1, pp. 1–10, Jul. 1994, doi: 10.1007/BF01414626.